The Astrophysical Journal Supplement Series, 184:158–171, 2009 September doi:10.1088/0067-0049/184/1/158

THE *CHANDRA* COSMOS SURVEY. I. OVERVIEW AND POINT SOURCE CATALOG

Martin Elvis[1], Francesca Civano[1], Cristian Vignali[2,3], Simonetta Puccetti[4,5], Fabrizio Fiore[5], Nico Cappelluti[6], T. L. Aldcroft[1], Antonella Fruscione[1], G. Zamorani[3], Andrea Comastri[3], Marcella Brusa[6,7], Roberto Gilli[3], Takamitsu Miyaji[8,9,30], Francesco Damiani[10], Anton M. Koekemoer[11], Alexis Finoguenov[6,7], Hermann Brunner[6], C.M. Urry[12], John Silverman[13], Vincenzo Mainieri[14], Guenther Hasinger[6,15], Richard Griffiths[16], Marcella Carollo[13], Heng Hao[1], Luigi Guzzo[17], Andrew Blain[18], Daniela Calzetti[19], C. Carilli[20], Peter Capak[21], Stefano Ettori[3], Giuseppina Fabbiano[1], Chris Impey[22], Simon Lilly[13], Bahram Mobasher[23], Michael Rich[24], Mara Salvato[18], D.B. Sanders[25], Eva Schinnerer[26], N. Scoville[18], Patrick Shopbell[18], James E. Taylor[27], Yoshiaki Taniguchi[28], and Marta Volonteri[29]

[1] Harvard-Smithsonian Center for Astrophysics, 60 Garden St., Cambridge, MA 02138, USA
[2] Dipartimento di Astronomia, Università degli Studi di Bologna, Via Ranzani 1, I-40127 Bologna, Italy
[3] INAF—Osservatorio Astronomico di Bologna, Via Ranzani 1, I-40127 Bologna, Italy
[4] ASI Science Data Center, via Galileo Galilei, 00044 Frascati, Italy
[5] INAF−Osservatorio astronomico di Roma, Via Frascati 33, 00040 Monteporzio Catone, Italy
[6] Max-Planck-Institute für Extraterrestrische Physik, Postfach 1312, 85741, Garching bei München, Germany
[7] University of Maryland, Baltimore County, 1000 Hilltop Circle, Baltimore, MD 21250, USA
[8] Instituto de Astronomía, Universidad Nacional Autónoma de México, Ensenada, Mexico
[9] Center for Astrophysics and Space Sciences, University of California San Diego, Code 0424, 9500 Gilman Drive, La Jolla, CA 92093, USA
[10] INAF—Osservatorio Astronomico di Palermo, Piazza del Parlamento 1, I-90134 Palermo, Italy
[11] Space Telescope Science Institute, 3700 San Martin Drive, Baltimore, MD 21218, USA
[12] Department of Physics and Yale Center for Astronomy & Astrophysics, Yale University, P.O. Box 208121, New Haven, CT 06520-8121, USA
[13] Department of Physics, Eidgenössische Technische Hochschule-Zurich, CH-8093 Zurich, Switzerland
[14] ESO, Karl-Schwarschild-Strasse 2, D–85748 Garching, Germany
[15] Max-Planck-Institute für Plasmaphysik, Boltzmannstrasse 2, D-85748 Garching bei München, Germany
[16] Department of Physics, Carnegie Mellon University, 5000 Forbes Avenue, Pittsburgh, PA 15213, USA
[17] INAF—Osservatorio Astronomico di Brera, via Bianchi 46, 23807 Merate, Italy
[18] California Institute of Technology, MC 105-24, 1200 East California Boulevard, Pasadena, CA 91125, USA
[19] Department of Astronomy, University of Massachusetts, Amherst, MA 01003, USA
[20] National Radio Astronomy Observatory, PO Box O, Socorro NM 87801, USA
[21] Spitzer Science Center, 314-6 Caltech, Pasadena, CA 91125, USA
[22] Steward Observatory, University of Arizona, 933 North Cherry Avenue, Tucson, AZ 85721, USA
[23] Department of Physics and Astronomy, University of California, Riverside, CA 92521, USA
[24] Department of Physics and Astronomy, University of California, Los Angeles, CA 90095, USA
[25] Institute for Astronomy, University of Hawaii, 2680 Woodlawn Dr., Honolulu, HI 96822, USA
[26] Max-Planck-Institut für Astronomie, Königstuhl 17, Heidelberg D-69117, Germany
[27] Department of Physics and Astronomy, University of Waterloo, Waterloo, Ontario, N2L 3G1, Canada
[28] Research Center for Space and Cosmic Evolution, Ehime University, Bunkyo-cho 2-5, Matsuyama 790-8577, Japan
[29] Department of Astronomy, University of Michigan, Ann Arbor, MI 48109, USA
Received 2008 November 4; accepted 2009 July 29; published 2009 August 27

ABSTRACT

The *Chandra* COSMOS Survey (C-COSMOS) is a large, 1.8 Ms, *Chandra* program that has imaged the central 0.5 deg^2 of the COSMOS field (centered at 10^h, $+02^o$) with an effective exposure of ∼160 ks, and an outer 0.4 deg^2 area with an effective exposure of ∼80 ks. The limiting source detection depths are 1.9×10^{-16} erg cm^{-2} s^{-1} in the soft (0.5–2 keV) band, 7.3×10^{-16} erg cm^{-2} s^{-1} in the hard (2–10 keV) band, and 5.7×10^{-16} erg cm^{-2} s^{-1} in the full (0.5–10 keV) band. Here we describe the strategy, design, and execution of the C-COSMOS survey, and present the catalog of 1761 point sources detected at a probability of being spurious of $<2 \times 10^{-5}$ (1655 in the full, 1340 in the soft, and 1017 in the hard bands). By using a grid of 36 heavily (∼50%) overlapping pointing positions with the ACIS-I imager, a remarkably uniform (±12%) exposure across the inner 0.5 deg^2 field was obtained, leading to a sharply defined lower flux limit. The widely different point-spread functions obtained in each exposure at each point in the field required a novel source detection method, because of the overlapping tiling strategy, which is described in a companion paper. This method produced reliable sources down to a 7–12 counts, as verified by the resulting log$N$–log$S$ curve, with subarcsecond positions, enabling optical and infrared identifications of virtually all sources, as reported in a second companion paper. The full catalog is described here in detail and is available online.

Key words: catalogs – cosmology: observations – galaxies: evolution – quasars: general – surveys – X-rays: general

Online-only material: color figures, supplementary data

1. INTRODUCTION

The co-evolution of galaxies and quasars or active galactic nuclei (AGNs) has been vigorously pursued both observationally

[30] Address for correspondence: P.O. Box 439027, San Ysidro, CA 92143-9027, USA.

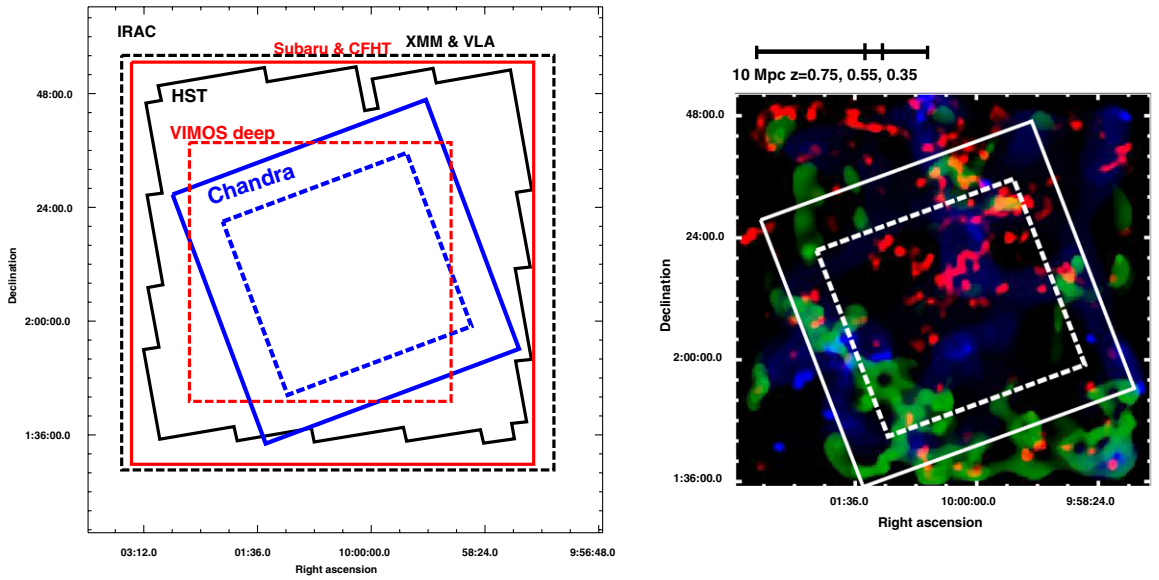

Figure 1. Left: map of the COSMOS field showing the coverage at various wavelengths: the IRAC 3.6 μm mosaic is the background image; blue solid = *Chandra*, blue dashed = *Chandra* deep; black polygon = *HST*; red solid = Subaru, CFHT, zCOSMOS bright; red dashed = zCOSMOS deep; black dashed = *XMM* and VLA. The *Spitzer* MIPS observations cover an area two times larger. Right: LSS seen in galaxy distributions in the COSMOS field (Scoville et al. 2007c), ranging in size from 1–20 Mpc, based on photo-z's accurate to $\sim$1%. Blue is centered on $z = 0.35$, green on $z = 0.55$, and red on $z = 0.75$, each with $\Delta z = 0.05$. The C-COSMOS field outline is shown as the white tilted square, with the dashed line delineating the high exposure area as in the left panel. A scale showing 10 Mpc at the three redshifts is shown at the top. In both panels north is up, east is to the left.

and theoretically for a decade, ever since the discovery that the mass of the central black hole is tightly correlated both with the luminosity (Magorrian et al. 1998; Marconi & Hunt 2003) and the velocity dispersion of the spheroid (M_{BH}–σ relation; Ferrarese & Merrit 2000; Gebhardt et al. 2000; Tremaine et al. 2002). Tackling this large subject requires the study of both galaxies and AGNs back to the epoch when both were growing rapidly, i.e. $z \sim$ 1–3, requiring deep observations across many wavelengths, from radio through the infrared, optical and ultraviolet, to the X-rays. At the same time, the wide range of cosmic density and the rapid changes in this large-scale structure (LSS) require wide field observations that sample the universe at close to their true fractions.

The Cosmic Evolution Survey (COSMOS; Scoville et al. 2007a) is a deep and wide extragalactic survey designed to have sufficient area to overcome most cosmic variance, which requires sampling regions some 50 Mpc on a side (Figure 1; Scoville et al. 2007a), and with sufficient depth to sample the z = 1–3 galaxy and AGN population. The contiguous 2 deg^2 COSMOS field samples a volume of $\sim 6 \times 10^6$ Mpc^3 at z = 0.5–1 (Wright 2006). This is $\sim$10% of the volume imaged by the Sloan Digital Sky Survey (SDSS) in the local ($z < 0.1$) universe (5.7×10^7 Mpc^3, 8000 deg^2, DR5[31]). COSMOS is a region of low, uniform, Galactic obscuration ($E(B-V) \simeq 0.02$ mag, N_H (2.7×10^{20} cm^{-2}; Dickey & Lockman 1990). COSMOS is likely to be the largest survey of this type for the next decade.

The location of the COSMOS area near the equator (10^h, +02°) allows all major and future facilities[32] (notably EVLA, ALMA, and SKA) to target this region down to faint limits (Scoville et al. 2007a). Space-based imaging has been undertaken in the F840W ($\sim i$-band) with the *Hubble Space Telescope* (*HST*, Scoville et al. 2007b), in the 3.5 μm–70 μm infrared using *Spitzer* IRAC and MIPS (Sanders et al. 2007), in the UV using the *Galaxy Evolution Explorer* (*GALEX*; Zamojski et al. 2007), and in 0.5–10 keV X-rays with *XMM* (Hasinger et al. 2007; Cappelluti et al. 2007). Ground-based imaging spans the radio (1400 MHz VLA; Schinnerer et al. 2007), the near-IR with CTIO and KPNO (Capak et al. 2007) and CFHT (McCracken et al. 2009), the optical to AB$\sim$26–27 with *Subaru* in 21 bands (Taniguchi et al. 2007). Finally, large dedicated ground-based spectroscopy programs in the optical with Magellan/IMACS (Trump et al. 2007) and VLT/VIMOS (Lilly et al. 2007) are well under way.

This wealth of data has resulted in an initial 15-band photometric catalog of $\sim 10^6$ objects (Capak et al. 2007) from which photometric redshifts good to $<$3% for $z < 1.2$ and $r < 24$ have been derived (Mobasher et al. 2007). Recently, more photometric bands have been added, resulting in improved photo-z's for the galaxy population accurate to $\Delta z/(1+z) < 1\%$ (Ilbert et al. 2008) and to $\Delta z/(1+z) \sim 2\%$ for the AGN population (Salvato et al. 2009).

We have undertaken the *Chandra*-COSMOS survey (C-COSMOS) to cover the central 0.9 deg^2 region of the COSMOS field (Figure 1, left), containing a wide range of cosmic overdensity (Figure 1, right), with the ACIS-I CCD imager (Garmire et al. 2003) on board the *Chandra X-ray Observatory* (Weisskopf et al. 2002). The survey took 1.8 Ms of *Chandra* observing time ($\sim$21 days) and was the largest guest observer program approved in a single AO at the time it was undertaken (2006 November–2007 June). C-COSMOS employed a series of 36 heavily overlapped ACIS-I 50 ks pointings to give an exposure of $\sim$160 ks over the inner area to a depth of $\sim 1.9 \times 10^{-16}$ erg cm^{-2} s^{-1} (0.5–2 keV), providing an unprecedented combination of contiguous area and depth in the X-ray band. This overlapping tiling strategy gives highly uniform exposure, and so a well-defined flux limit.

Several of the deepest COSMOS surveys are now concentrating on this same central subfield of COSMOS: the z-COSMOS Deep spectroscopic survey (to $B \sim 25$; Lilly et al. 2007), the deep VLA survey (6 μJy rms; E. Schinnerer et al. 2009, in

[31] http://www.sdss.org/dr5/
[32] Except for those in Antarctica.

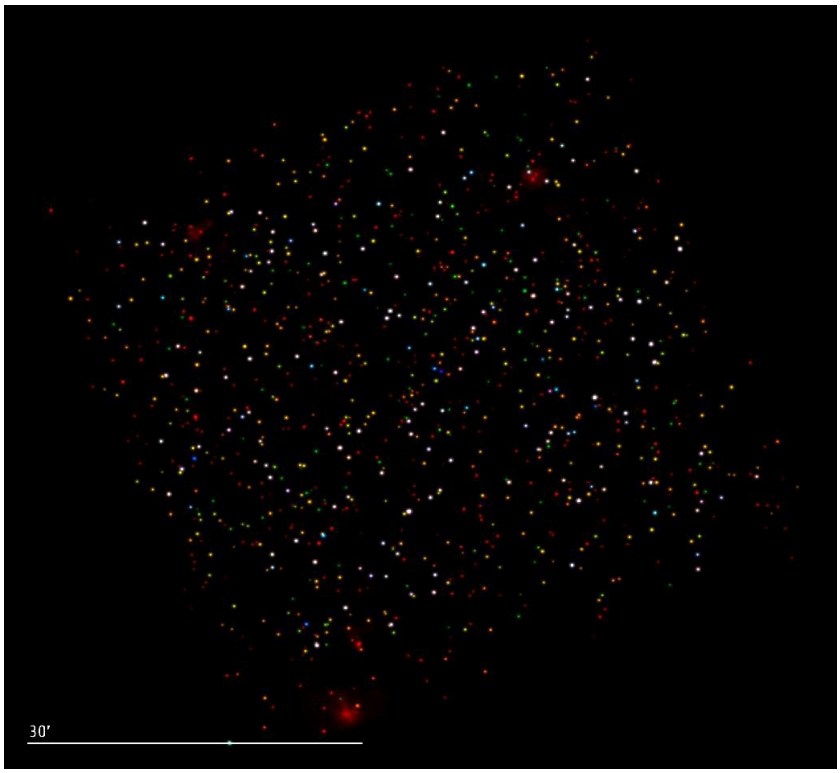

Figure 2. X-ray image of the *Chandra* COSMOS field, optimized to show point sources with a wide variety of X-ray colors. A scale showing 30 arcmin (the approximate diameter of the full moon) is shown for comparison. North is at the top; east is to the left. The full angular resolution of *Chandra* is not well represented in this image as, in order to display the point sources clearly, the original image has been smoothed with a sharp Gaussian with radius equal to 2.″9, and added to an image of the field smoothed with a wide Gaussian with radius equal to 4.″4. X-ray "colors" are mapped so that red is the 0.5–2 keV band, green is the 2–4.5 keV band, blue is the 4.5–7 keV band, and each energy band was smoothed in the same way. Selected prominent clusters have been adaptively smoothed for display (red extended shapes).

preparation), and several millimeter and submillimeter surveys (MAMBO, Bertoldi et al. 2007 and AzTEC, Scott et al. 2008). GALEX has observed the central field deeply (Zamojski et al. 2007) and is currently monitoring this area. The Ultra-VISTA survey will undertake a deep *yJHK* survey of the central 1.5 deg^2, half of which will be surveyed to the unprecedented limits of ∼26 AB mag (Arnaboldi et al. 2007).

By going for large area rather than extreme depth, most of the C-COSMOS sources are sufficiently bright to be detected in the rest of the pan-chromatic COSMOS data set, allowing rapid identifications (F. Civano et al. 2009, in preparation) and determination of their multiwavelength properties (e.g., M. Elvis et al. 2009, in preparation). On the other hand, C-COSMOS is sufficiently deep that significant numbers of normal and starburst galaxies with luminosity of 10^{42} erg s^{-1} can be detected up to $z \sim 0.9$, a redshift depth comparable with that of the galaxy redshift surveys in the COSMOS field (Taniguchi et al. 2007; Lilly et al. 2007). Adding the *Chandra* coverage to the COSMOS survey adds a valuable resource for the study of the co-evolution of black holes and their host galaxies, of the spectral energy distributions of faint quasars and active galactic nuclei, and the evolution of galaxies.

The summed image of the entire C-COSMOS field is shown in Figure 2, where colors have been mapped to X-ray bands.

This is the first of three papers presenting the basic results of the C-COSMOS survey over the whole field. Paper I (this paper) reports on the strategy, design, and execution of the C-COSMOS survey, and present the catalog of 1761 point-like X-ray sources detected in C-COSMOS; Paper II (Puccetti et al. 2009) presents the details of the simulations carried out to optimize the source detection method; Paper III (F. Civano et al. 2009, in preparation) presents the identification of the X-ray sources with optical and infrared counterparts. We conclude by listing the primary science objectives foreseen for the C-COSMOS data. Papers on several of these topics are in preparation.

We assume a ΛCDM cosmology with $H_0 = 70$ km s^{-1}, $\Omega_m = 0.27$, $\Omega_{\rm vac} = 0.73$.

2. THE *CHANDRA* COSMOS STRATEGY

For C-COSMOS we have developed a strategy that uses ∼50% overlapping tiling of the 16.9 × 16.9 arcmin ACIS-I fields. This tiling produces a remarkably uniform sensitivity in the central part of the field, and a well-defined flux limit with a sharp cutoff (Figure 3; for details on the generation of sensitivity maps, see Section 7 in Paper II). This approach also ensures that the area with HPD < 2″ is maximized, so that the unique *Chandra* high resolution imaging (van Speybroeck et al. 1997) can be exploited fully, albeit with 1/4 of the exposure time. The good *Chandra* point-spread function (PSF) resolves sources 2″ apart over ∼0.7 deg^2, corresponding to 8–16 kpc separations for $z = 0.3$–0.9, and locates point sources to <4 kpc at *any redshift*. Thus close mergers can be resolved, and nuclear sources distinguished from off-nuclear sources in galaxies (Ultra-luminous X-ray Sources, ULXs; Fabbiano 2006, Lehmer et al. 2006; Mainieri et al. 2009).

Point source detection sensitivities were estimated for three standard *Chandra* bands: soft (S, 0.5–2 keV), hard (H, 2–10 keV), and full (F, 0.5–10 keV). Due to the high background

Table 1
C-COSMOS Flux Limits and Corresponding *XMM*-COSMOS Flux Limits

Band	C-COSMOS(lim)[a]	C-COSMOS(log N–log S)[a]	*XMM*-COSMOS[a]
Soft (0.5–2 keV)	1.9	2.5	5
Hard (2–10 keV)	7.3	16	25
Full (0.5–10 keV)	5.7	...	...

Note.
[a] Flux limits are reported in units of 10^{-16} erg cm^{-2} s^{-1}, for bands up to 10 keV, but were measured only up to 7 keV. (See text for details.)

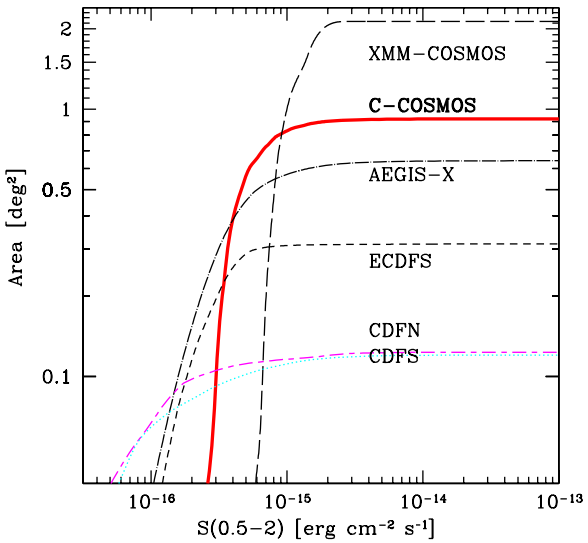

Figure 3. Area–flux curve for C-COSMOS (red solid line; 0.5–2 keV). The coverage of ECDFS (Lehmer et al. 2005; dashed line), AEGIS-X (Laird et al. 2008; dash-dotted line), CDFN (Alexander et al. 2003; magenta short-long dashed line), CDFS (Luo et al. 2008; cyan dotted line), and *XMM*-COSMOS (Cappelluti et al. 2009; black dashed line) are shown for comparison.

(A color version of this figure is available in the online journal.)

in the 7–10 keV energy range,[33] channels above 7 keV were not used for source detection. (See Section 4.2.2 and Paper II for details). The C-COSMOS flux limits in three bands are reported in Table 1, together with the *XMM*-COSMOS limits for comparison: C-COSMOS sensitivity is three times below the corresponding flux limits for the *XMM*-COSMOS survey (dashed line; Cappelluti et al. 2009), making them complementary surveys.

The achieved sensitivity–area curve[34] (Figure 3) has a sharp cutoff at low fluxes.

The C-COSMOS soft band flux limit corresponds to luminosities of (0.8, 4, 11)$\times 10^{41}$ erg s^{-1} at z = (0.3, 0.6, 0.9) respectively, while the hard band flux limit corresponds to four times higher luminosities. Both luminous elliptical galaxies and starbursts often exceed these luminosities, and starburst galaxies are known to become common (Hornschemeier et al. 2003) at these X-ray fluxes.

The low ACIS background enables stacking analysis, in which counts at the positions of known classes of objects, e.g. subsets of the thousands of galaxies with redshifts, are co-added to increase the effective exposure time (Brusa et al. 2002; Hornschemeier et al. 2002; Brandt et al. 2001; Nandra et al. 2002; Fiore et al. 2008).

[33] http://cxc.harvard.edu/contrib/maxim/bg/index.html#spec
[34] This curve is remarkably close to the predictions from the proposal, reflecting the high accuracy with which the requested tiling was executed.

Table 2
Coordinates of the C-COSMOS Field, Center, and Corners of the Outer and Inner Regions, Clockwise from the NE (Top Left)

R.A.	Decl.
Center	
$10^h\ 00^m\ 24^s$	$+02^\circ\ 10'\ 55''$
Outer region	
$10^h\ 02^m\ 45^s$	$+02^\circ\ 26'\ 47''$
$09^h\ 59^m\ 11^s$	$+02^\circ\ 46'\ 45''$
$09^h\ 57^m\ 54^s$	$+01^\circ\ 53'\ 00''$
$10^h\ 01^m\ 23^s$	$+01^\circ\ 33'\ 59''$
Inner region	
$10^h\ 02^m\ 05^s$	$+02^\circ\ 21'\ 13''$
$09^h\ 59^m\ 30^s$	$+02^\circ\ 35'\ 47''$
$09^h\ 58^m\ 35^s$	$+01^\circ\ 59'\ 19''$
$10^h\ 01^m\ 11^s$	$+01^\circ\ 44'\ 37''$

2.1. Design

The C-COSMOS tiling scheme (Figure 4, left panel) covers the central area of the COSMOS field in the most efficient manner that we could devise. A 6 × 6 raster array of 36 ACIS-I pointings (one ACIS pointing field of view is outlined in black in Figure 4, left), each of 50 ks nominal exposure, were chosen. The center of the array (Table 2) is slightly offset from the center of the COSMOS field to match the z-COSMOS deep field (Lilly et al. 2007).

The value of the 8.′0 offset between pointing centers was chosen to be slightly less than the 8.′3 size of an ACIS chip (Garmire et al., 2003; *Chandra* Proposers' Observatory Guide, aka POG, 2007[35]; Table 6.1), so that chip gaps are not co-added to create small scale dips in the effective exposure time.

The inner part of the field was covered by four exposures, to give a total nominal exposure of 200 ks (effective exposure ∼160 ks) over a $42' \times 42'$ area (0.5 deg^2, green area in Figure 4). The outer region has been covered by two observations (blue area) and the four corners covered by 1 observation (purple area). The corners of the outer and inner regions are reported in Table 2 clockwise from the top left.

Sources at a flux of $\sim 2.0 \times 10^{-16}$ erg cm^{-2} s^{-1} (0.5–2 keV) have a total of 5–10 summed counts in the four exposures, ensuring a good detection, given the low *Chandra*/ACIS background of ∼2 counts/200 ks over a 2 arcsec radius circle (see Section 4.2.1).

The heavily overlapped tiling scheme produces a smooth exposure map that is flat to 12% in the central region (see Figure 4, right panel and Section 4.2.2).

2.2. Comparison with Other Legacy Surveys

Chandra observing time has been dedicated to several large legacy surveys: CDF-S (Giacconi et al. 2002; Luo et al. 2008),

[35] *Chandra* X-ray Center publication TD 403.00.010.

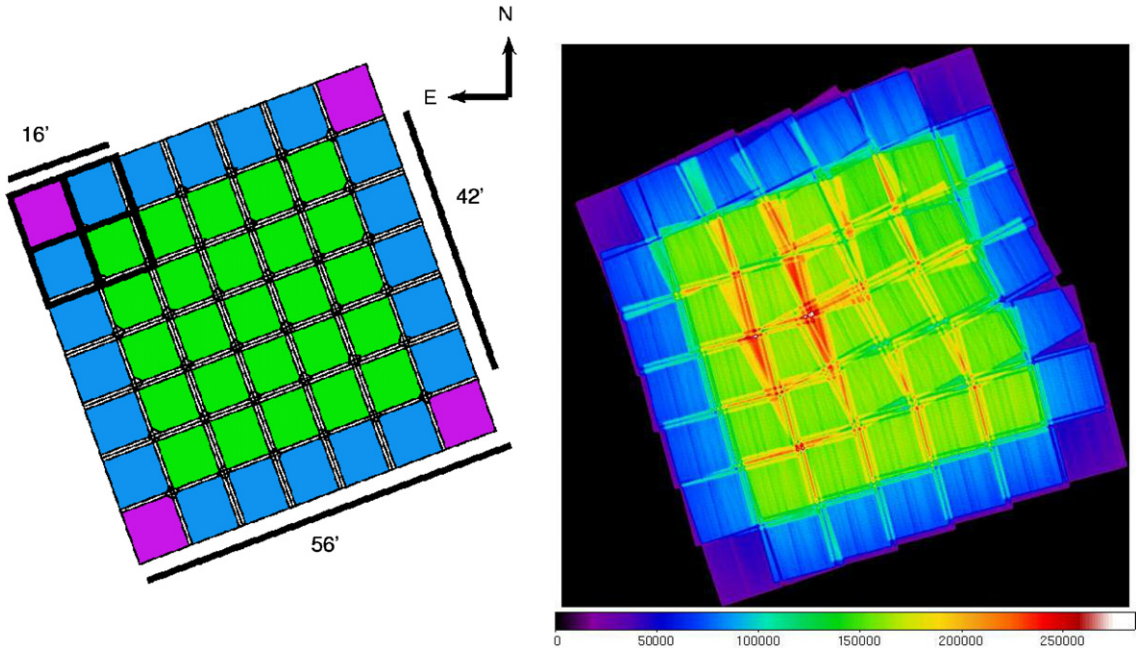

Figure 4. Left: the "as designed" C-COSMOS tiling for the 36 50 ks pointings. The thick black box (top left) represents one ACIS-I pointing, the thin boxes all the pointings. Different colors show areas with different number of overlapping pointings: green—4 overlapping pointings; blue—2 overlapping pointings; purple—1 pointing. The black bars show roughly the relative dimensions of one pointing (∼16′), of the inner area with larger exposure (∼42′), and of the total field (∼56′). Raster point (see Table 3) 1–1 lies at the top right (NE) and 1–6 lies at the top left (NW). Right: the "as executed" exposure map for the C-COSMOS survey in the soft band. The color bar gives the achieved effective exposure in units of seconds.

CDF-N (Alexander et al. 2003), ECDF-S (Lehmer et al. 2005), AEGIS-X (Nandra et al. 2005; Laird et al. 2008), and XBootes (Murray et al. 2005). These surveys have different emphases in area and depth, so we summarize the special features of C-COSMOS here.

Like all contiguous area surveys, C-COSMOS has significant advantages over noncontiguous surveys (e.g., SEXSI, Harrison et al. 2003, Eckart et al. 2006; ChaMP, Kim et al. 2007), because of the difficulty of getting deep multiwavelength coverage of noncontiguous fields.

C-COSMOS is neither the deepest (CDFN and CDFS) nor the widest (XBootes) legacy *Chandra* survey. A comparable sensitivity has been reached in the somewhat smaller AEGIS field (the dot-dashed line in Figure 3; Laird et al. 2008). C-COSMOS differs from the other surveys by having the largest area at fluxes (3–10) $\times$ 10^{-16} erg cm^{-2} s^{-1} (*S* band), and a sharper low flux limit cutoff in the area surveyed than most other recent X-ray surveys. The single field CDF-S and CDF-N have notably shallower roll-offs in their sensitivity curves (magenta and blue lines in Figure 3).

X-ray surveys are normally compared using an "area-depth" plot (e.g., Brandt & Hasinger 2005). The differences in cutoff sharpness noted above require a slight revision of this plot to compare C-COSMOS with comparable contiguous *Chandra* and *XMM-Newton* surveys self-consistently. This is because the area normally quoted is the maximum area of the survey, while the normally quoted flux limit is that of the faintest source in the survey, which in most cases can be detected only in a much smaller area. If all surveys have similar cutoffs the difference is qualitatively unimportant, but in the case of C-COSMOS it makes a substantial difference.

We have used the area–flux curve of each survey to derive the flux at the point where each survey reaches 80% of the maximum survey area. We plot these values in Figure 5 (filled circles) for the *Chandra* contiguous area surveys (CDFN, Alexander et al. 2003; CDFS, Luo et al. 2008; ECDFS, Lehmer et al. 2005; AEGIS- X, Laird et al. 2008; XBootes, Murray et al. 2005; ELAIS-N, Manners et al. 2003), and for the *XMM-Newton* contiguous surveys that fill regions of the flux-area plane (ELAIS-S1, Puccetti et al. 2006; *XMM*-COSMOS, Cappelluti et al. 2009; Lockman-Hole, Brunner et al. 2008). The C-COSMOS flux at 80% of the area covered (0.72 deg^2) in the soft band is 6×10^{-16} erg cm^{-2} s^{-1}.

Compared with other plots of this kind (e.g., Brandt & Hasinger 2005) the points in Figure 5 tend to be moved diagonally toward smaller area and high flux limits. This shift can be quite large for surveys with shallow slopes at low fluxes in their area–flux limit curves (such as, for example, the deep fields).

Curves of constant numbers of sources (for the soft band) are shown in Figure 5 following the predictions of the Gilli et al. (2007) XRB model.[36] The larger source numbers in XBootes and in the two COSMOS surveys are notable. Some soft band 1000 sources are predicted for C-COSMOS above the "80% area" flux limit, while 1023 are actually detected.

The total number of sources in the CDF fields is, of course, significantly larger than the "80% area" number The more sensitive, smaller area, parts of each survey add more sources than indicated by the dashed black lines, especially for the curves that have shallow cutoffs. To clarify this quite important point, Figure 5 also shows the area–flux curves for each survey down to their "20% area" value. These curves show the differences between the surveys' flux limits. The differences between the two CDF deep fields are quite striking and are due to the slightly different observational strategies used for the two surveys (changing only the roll angle (CDF-N), or also moving the field center (CDF-S)). The figure caption gives both the 80% area

[36] The curves have been computed using the tool "POrtable Multi Purpose Application for XRB and AGN counts" available at the Web site http://www.bo.astro.it/∼gilli/counts.html. We have checked that the numbers in each survey at the quoted 80% area flux levels agree with these curves.

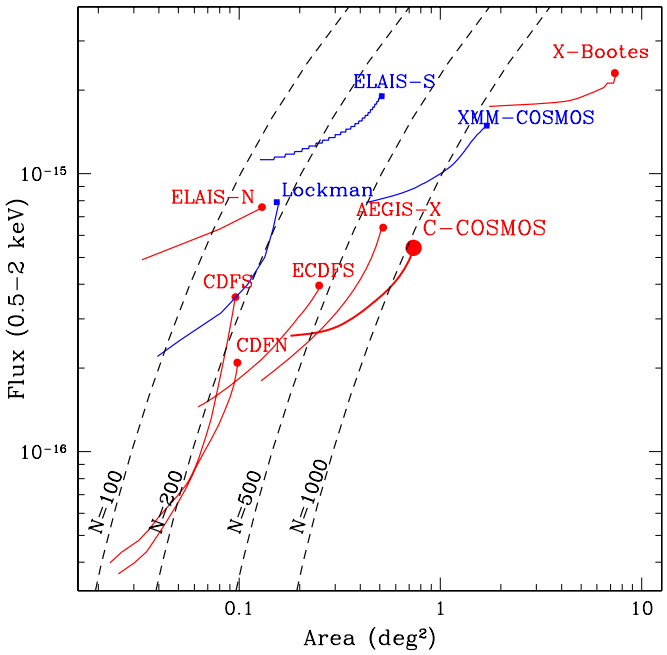

Figure 5. Area–flux curves for *Chandra* (red) and *XMM-Newton* (blue) contiguous X-ray surveys. Each survey has been plotted using each sensitivity curve starting from the flux corresponding to the area that is 80% of the maximum area for that survey (large points at the top of each curve), to the flux corresponding to the 20% of the total area (bottom of each curve). Data were taken from the following *Chandra* references: XBootes ($N(80) = 3963$, $N(\mathrm{total}) = 3180$)—Murray et al. 2005; CDFN ($N(80) = 221$, $N(\mathrm{total}) = 451$)—Alexander et al. 2003; CDFS ($N(80) = 184$, $N(\mathrm{total}) = 392$)—Luo et al. 2008; ECDFS ($N(80) = 411$, $N(\mathrm{total}) = 598$)—Lehmer et al. 2005; AEGIS-X ($N(80) = 689$, $N(\mathrm{total}) = 1032$)—Laird et al. 2008; ELAIS-N ($N(80) = 156$, $N(\mathrm{total}) = 182$)—Manners et al. 2003; and *XMM-Newton* references: *XMM*-COSMOS ($N(80) = 1200$, $N(\mathrm{total}) = 1621$)—Cappelluti et al. 2009; Lockman ($N(80) = 195$, $N(\mathrm{total}) = 340$)—Brunner et al. 2008; ELAIS-S ($N(80) = 319$, $N(\mathrm{total}) = 395$)—Puccetti et al. 2006, C-COSMOS ($N(80) = 1070$, $N(\mathrm{total}) = 1340$)—this paper, where "$N(80)$" is the number of S band sources at the 80% area fluxl, and "$N(\mathrm{total})$" is the total number of S-band sources in the survey. The black dashed curves show the total number of 0.5–2 keV sources expected based on the log$N$-log$S$ relation predicted by Gilli et al. (2007) at the 80% area point. Each survey contains more sources at fainter fluxes and from smaller areas. The more vertical the sensitivity curve, the more of these fainter sources will be found.

(A color version of this figure is available in the online journal.)

and the total number of soft band sources for each survey and shows how the different area–flux curves affect the number of sources. The AEGIS-X survey (Laird et al. 2008), for example, has about double the number of S-band sources predicted at the 80% point, as do the two CDF fields. Instead, C-COSMOS, with a flatter flux-area curve, has ∼30% more S-band sources in total than the 80% area number.

Each of these surveys has extended multiwavelength coverage, but C-COSMOS is the only deep and wide X-ray survey field selected for both existing deep multiwavelength coverage, and for future legacy value, due to the equatorial location of the COSMOS field. The AEGIS field ($\delta = +52°$), the CDF-N field ($\delta = +62°$), and the XBootes field ($\delta = +35°$) are all too northerly to be accessible by ALMA or the VLT. The COSMOS field was also selected to have low IR cirrus emission, and a lack of bright stars, X-ray or radio sources in the field to maximize multiwavelength coverage.

C-COSMOS and *XMM*-COSMOS complement one another by providing large samples of sources over a wide flux range (Figure 8), while sharing the same extensive multiwavelength data set. *XMM*-COSMOS provides a larger sample of extended sources, while C-COSMOS provides a larger sample of starburst and normal galaxies.

3. OBSERVATIONS

A summary of the *Chandra* ACIS-I C-COSMOS observations as carried out is given in Table 3. Primarily because of thermal constraints on spacecraft components (POG; Section 3.3.3), many of the 36 C-COSMOS pointings were scheduled as two or more separate ObsIDs, giving 49 C-COSMOS observations in all. The indices X–Y (1–1 through 6–6) describe the field numbers, where X is an index in R.A. and Y an index in decl., with 1–1 being in the top right (NE) corner of Figure 4 (left panel), and 1–6 being in the top left (NW) corner.

The observations took place in two main blocks: 2006 December–2007 January and 2007 April–June (Table 3). The fields were observed at nominal roll angles of 250/70 deg, where the visibility of the COSMOS field is at maximum (∼70%) and the pitch angle is such that the constraints are either unrestricted or restricted only to avoid overheating of the charged particle detector (EPHIN). As an equatorial field, the roll angle of the COSMOS field is quite stable (55.2–69.6, 248.4–256.2) for periods of ∼100 days. As a result, the *Chandra X-ray Center* (CXC) Mission Planning team were able to maintain a tight roll angle range of ±6° around the nominal values (Table 3), leading to a highly uniform exposure of the whole field.

The mean effective exposure time per field (not per ObsID) is 46.3 ks, when only the good time intervals (GTIs), cleaned of the few high background times (Section 4.2.1), are used.[37] The maximum exposure is 48.3 ks and the minimum exposure (excluding a single 37.6 ks exposure for field 2–5, Table 3) is 44.1 ks. So, with this exception, the range of exposures over the fully covered inner region varies by just ±2.0 ks (4%).

4. DATA PROCESSING

The data from the 49 obsids were uniformly processed in two phases using the CIAO 3.4 software tools[38] (Fruscione et al. 2006), the *yaxx*[39] tool and custom versions of the *XMM* SAS detect tool EMLDETECT.[40] Standard Level-1 and Level-2 processing pipeline[41] (ASCDS version 7.6.9) from the CXC were used. In the first processing phase we determined astrometric corrections (see below) for each ObsID. These corrections were then applied in the second phase where we reprocessed all event data starting with Level-1 products.

Data processing involved the following series of steps, as summarized below:

1. Astrometric corrections (<1.″1) to the standard COSMOS frame starting with the CXC supplied standard data products (Section 6);
2. Baseline data product creation by reprocessing all ObsIDs to a standard frame of reference using the new astrometry and standard CXC pipelines (Section 4.2);
3. Background reduction using high background time filtering (which affects only two ObsIDs) (Section 4.2.1);

[37] This is ∼93% of the requested exposure, well within the 90% tolerance limit defined for *Chandra* scheduling.
[38] http://cxc.harvard.edu/ciao/
[39] http://cxc.harvard.edu/contrib/yaxx/
[40] http://xmm.esac.esa.int/sas/8.0.0/EMLdetect
[41] Pipeline processing levels are explained at http://cxc.harvard.edu/ciao/data/sdp.html.

Table 3
Chandra-COSMOS Observation Summary

Obs. ID	Field	Obs. Start (UT)	Exp. Time[a] (ks)	R.A. (J2000.0)	Decl. (J2000.0)	Roll (deg)
7995	1–1	2007 Jun 01, 03:41	44.6	10 02 02.05	+02 22 36.46	248.4
7996	1–2	2006 Dec 28, 11:28	44.7	10 01 31.99	+02 25 20.48	63.4
7997	1–3	2006 Dec 30, 21:10	44.5	10 01 01.92	+02 28 04.50	62.8
8494	1–4	2006 Dec 16, 13:21	20.2	10 00 31.85	+02 30 48.52	66.4
8122	1–4	2007 Jan 20, 10:15	28.0	10 00 31.85	+02 30 48.52	55.2
8493	1–5	2006 Dec 12, 18:07	19.3	10 00 01.79	+02 33 32.55	66.4
7998	1–5	2007 Jan 10, 21:41	26.9	10 00 01.79	+02 33 32.55	63.2
8478	1–6	2006 Nov 24, 10:17	17.6	09 59 31.72	+02 36 16.58	69.6
7999	1–6	2006 Nov 25, 09:24	29.0	09 59 31.72	+02 36 16.58	69.6
8000	2–1	2007 May 26, 20:23	45.2	10 01 51.10	+02 15 05.52	253.2
8001	2–2	2007 Apr 02, 03:42	47.3	10 01 21.03	+02 17 49.54	256.2
8123	2–3	2007 Apr 07, 13:40	48.3	10 00 50.97	+02 20 33.55	255.2
8002	2–4	2006 Dec 19, 04:57	28.5	10 00 20.90	+02 23 17.58	65.0
8496	2–4	2006 Dec 23, 12:05	17.8	10 00 20.90	+02 23 17.58	65.0
8003	2–5	2007 Apr 02, 17:53	37.6	09 59 50.83	+02 26 01.61	255.2
8004	2–6	2006 Nov 27, 02:25	15.3	09 59 20.76	+02 28 45.64	68.6
8482	2–6	2006 Dec 02, 09:05	10.2	09 59 20.76	+02 28 45.64	68.6
8483	2–6	2006 Dec 04, 03:02	21.3	09 59 20.76	+02 28 45.64	68.6
8005	3–1	2007 Apr 25, 02:42	30.8	10 01 40.15	+02 07 34.57	255.2
8552	3–1	2007 Apr 26, 09:33	14.4	10 01 40.15	+02 07 34.57	255.2
8124	3–2	2007 Apr 08, 03:42	31.1	10 01 10.08	+02 10 18.59	255.2
8549	3–2	2007 May 05, 17:17	17.2	10 01 10.08	+02 10 18.59	255.2
8503	3–3	2006 Dec 31, 10:18	20.0	10 00 40.02	+02 13 02.61	62.2
8006	3–3	2007 Jan 01, 11:48	25.8	10 00 40.02	+02 13 02.61	62.2
8007	3–4	2006 Dec 19, 22:18	21.1	10 00 09.95	+02 15 46.64	64.2
8497	3–4	2006 Dec 25, 01:50	27.1	10 00 09.95	+02 15 46.64	64.2
8008	3–5	2007 Jan 02, 04:39	45.0	09 59 39.88	+02 18 30.67	61.9
8009	3–6	2007 Jan 02, 18:06	44.8	09 59 09.81	+02 21 14.70	61.8
8010	4–1	2007 Apr 27, 18:45	32.9	10 01 29.19	+02 00 03.29	255.2
8553	4–1	2007 Apr 29, 01:02	14.4	10 01 29.19	+02 00 03.29	255.2
8011	4–2	2007 Apr 04, 04:08	45.8	10 00 59.13	+02 02 47.30	255.2
8012	4–3	2007 Jan 04, 05:30	48.0	10 00 29.06	+02 05 31.33	61.3
8013	4–4	2007 Jan 04, 19:44	46.9	09 59 58.99	+02 08 15.36	61.1
8014	4–5	2007 Jan 05, 09:29	44.2	09 59 28.92	+02 10 59.38	60.9
8015	4–6	2007 Jan 07, 09:53	44.1	09 58 58.85	+02 13 43.42	60.2
8550	5–1	2007 Apr 18, 19:11	22.7	10 01 18.25	+01 52 32.34	255.2
8016	5–1	2007 Apr 19, 20:24	23.3	10 01 18.25	+01 52 32.34	255.2
8017	5–2	2007 Apr 04, 17:55	45.3	10 00 48.18	+01 55 16.35	255.2
8018	5–3	2007 Apr 05, 07:17	45.8	10 00 18.11	+01 58 00.38	255.2
8019	5–4	2007 Apr 06, 23:25	48.0	09 59 48.04	+02 00 44.41	255.2
8020	5–5	2007 Apr 09, 06:12	47.8	09 59 17.97	+02 03 28.44	255.2
8021	5–6	2007 Apr 09, 20:24	47.3	09 58 47.90	+02 06 12.48	255.2
8022	6–1	2007 May 10, 23:28	30.9	10 01 07.30	+01 45 01.39	251.4
8555	6–1	2007 May 12, 16:06	16.2	10 01 07.30	+01 45 01.39	251.4
8023	6–2	2007 Apr 10, 12:49	48.3	10 00 37.24	+01 47 45.41	255.2
8024	6–3	2007 Apr 11, 21:40	47.9	10 00 07.17	+01 50 29.44	255.2
8025	6–4	2007 Apr 12, 11:57	47.9	09 59 37.10	+01 53 13.47	255.2
8026	6–5	2007 Apr 13, 07:31	45.8	09 59 07.03	+01 55 57.49	255.2
8027	6–6	2007 Apr 14, 13:54	48.3	09 58 36.96	+01 58 41.53	255.2

Note.
[a]After GTI and high-background filtering for two affected obsids. Intervals of 8.50 ks and 2.45 ks (respectively) were eliminated from the two affected ObsIDs (8003, 8014).

4. Exposure map creation in the three energy bands F, S, and H, using the standard CIAO tool sequence (Section 4.2.2);
5. Calculation of the sky coverage (i.e., the area covered to a given flux threshold) in the three energy bands, F, S, and H;
6. Candidate source detection using a wavelet technique (PWDetect; Damiani et al. 1997);[42]
7. Selection of reliable sources, with a probability of being spurious $<2 \times 10^{-5}$ in at least one band, using maximum likelihood fitting (EMLdetect) applied *simultaneously to each ObsID* at the positions of all candidate sources; Puccetti et al. (2009, Paper II) shows that EMLdetect reconstructs the input count rate of simulations well, while both PWDetect and detector underestimate the input count rate by about 15%;
8. Reliability checks for all sources using simulations, searches for outliers and visual checks (rejected

[42] We compared PWDetect with the CIAO tool wavdetect used by most *Chandra* deep surveys on a subset of C-COSMOS fields, and found no substantive difference in the results; PWDetect is a much faster algorithm, due to better memory buffering.

candidate sources were all in the wings of bright source PSFs);

9. Aperture photometry of reliable sources. At high fluxes the systematic error in the PSF, which is intrinsic to the EMLDETECT method, becomes larger than the statistical error; this systematic error is not present for aperture photometry;
10. Derivation of reliability and completeness criteria for the source catalog, leading to a log$N$–log$S$ curve that provides an end-to-end check of the source extraction by comparing with other surveys in the same flux range (Section 9).

Steps 1–4 are discussed more fully in the following subsections. Complete details of the steps from 5 onwards, including details of the simulations and tests, are given in Paper II.

4.1. Astrometry Corrections

In the first phase we determined accurate astrometric offsets for each ObsID. The good absolute astrometry produced by *Chandra* (0.″6 at 90% confidence, POG, Section 5) is still of the order of one ACIS pixel. To avoid a loss of sensitivity, correcting the astrometry to much less than one pixel error is needed before merging event files, or stacking.

To this end, we first produced a list of bright X-ray sources for each of the 49 ObsIDs, using the standard CIAO CELLDETECT tool. Starting with the standard ACIS Level-2 data products, we generated a broadband exposure map for each ACIS CCD using the CIAO[43] tools ASPHIST, MKINSTMAP, and MKEXPMAP. These exposure maps and event files were then used as input to a *Chandra*-adapted version of the *XMM*-SAS tool EMLDETECT (see the next section), with an input source candidate catalog obtained by running the sliding cell detection tool EBOXDETECT with a high threshold. All sources detected with likelihood parameter $\mathcal{L} > 10$ were compared with the CFHT MegaCam I-band catalog of the COSMOS field (Capak et al. 2007), selecting only the point-like sources with I magnitudes in the range 18–23. Using this restricted magnitude range minimizes systematic effects introduced by bright stars (saturation) and faint background objects (misidentification), and is appropriate for sources in this flux range (Brandt & Hasinger 2005). An optical–X-ray position correlation was computed using the likelihood algorithm included in the SAS task EPOSCORR (Cappelluti et al. 2007, 2009). This task uses all the possible counterparts of an X-ray source in the field to determine the most likely coordinate displacement. This method is independent of the actual spectroscopic identifications, but *post facto* all the identifications have proved to be correct (Paper III). No statistically significant offset in roll was required for any ObsID, so the change in roll was set to exactly zero. The systematic offsets between the X-ray and the optical positions were always smaller than 1.1 arcsec, with an average shift of ΔR.A. = 0.″04 and Δdecl. = 0.″25.

4.2. Baseline Data Products

The second phase of processing brought the 49 *Chandra* ObsIDs to a common reference frame using the offsets derived above, and generated the baseline data products that were then used as the starting point in all subsequent C-COSMOS analysis.

This processing was based on the CIAO thread for creating a new Level-2 event file from Level-1 products.[44] First, a new aspect solution for each ObsID was generated to remove the astrometric offset for each ObsID derived in above section, using the REPROJECT_ASPECT tool. Then a new bad pixel file was created using ACIS_RUN_HOTPIX (see "background reduction" below). Finally, a new ACIS Level-2 event file was then created for each ObsID using the ACIS_PROCESS_EVENTS tool, with (1) the standard *ASCA* grade set (grades [0, 2, 3, 4, and 6], POG Section 6.14), (2) pixel randomization turned off, (3) PHA randomization turned on, (4) very-faint mode processing enabled, and (5) the new aspect solution applied.

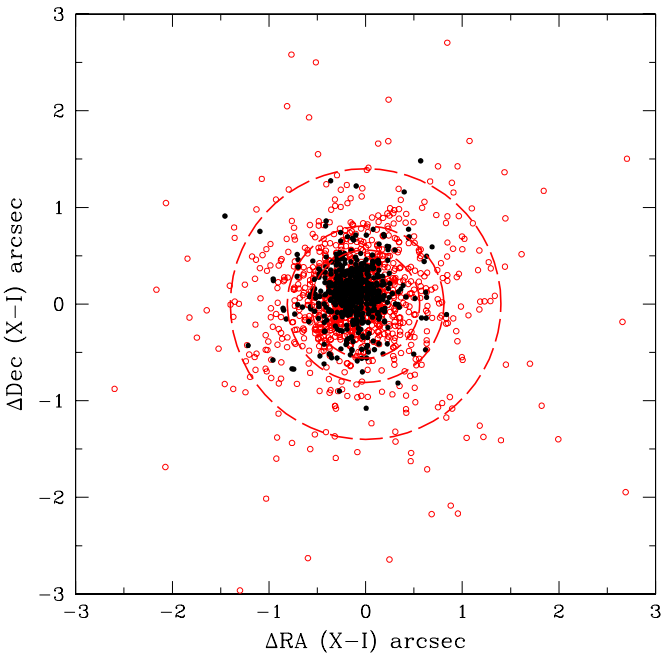

Figure 6. X-ray to I-band offsets (ΔR.A., Δdecl.) in arcsec for X-ray sources with a secure identification (F. Civano et al. 2009, in preparation) after the aspect correction described in the text has been applied (Section 4.1). The circles encompass 68% (0.″56), 90% (0.″81), and 95% (1.″41) of the sources with optical counterparts and secure identification. Red dots mark sources with less than 50 counts in the full band.

(A color version of this figure is available in the online journal.)

The astrometric corrections were checked using X-ray sources with point-like optical counterparts (F. Civano et al. 2009, in preparation, Paper III) that were *not* used to derive the offsets for the individual ObsIDs. The residual systematic shift (X-ray – optical position) is on average $\Delta\alpha = -0.''1$ and $\Delta\mathrm{dec} = 0.''08$, and the 1σ dispersion is 0.″56 (i.e., the radius within which 68% of sources lie; Figure 6). We find that 90% of the X-ray positions agree with the identified optical/IR counterpart positions to within 1.″1. The residual systematic shift is small enough that it will not affect the identification of any individual source and is smaller than the average X-ray positional error, and therefore has not been used to correct the astrometry any further. The good quality of the data provides positions with subarcsecond accuracy at off-axis angle $<6'$, in agreement with other *Chandra* surveys (0.″23–1.″90 in the CDFS, Luo et al. 2008; 0.″3–1.″67 in AEGIS, Laird et al. 2008).

4.2.1. Background Reduction and Cosmic Ray Afterglow Detection

Intervals of high background were determined by creating a background light curve for the ACIS-I CCD events with point sources found by WAVDETECT in the phase 1 processing removed. Only two obsids showed intervals with a significant

[43] http://cxc.harvard.edu/ciao/
[44] http://cxc.harvard.edu/ciao3.4/threads/createL2/

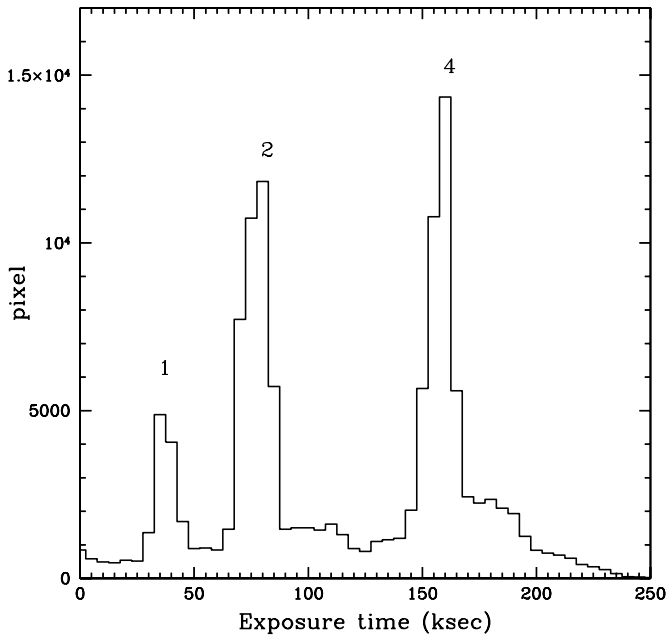

Figure 7. Histogram of the exposure times in the summed C-COSMOS field. The narrow peaks lie at the 1, 2, and 4 exposure values. The broader bases correspond to overlaps caused by slight variations in the roll angles of the ObsIDs.

Table 4
Conversion Factors from Count Rates in the Soft, Full, and Hard Bands (0.5–2, 0.5–7, 2–7 keV) to Fluxes in the Same Bands for Different Spectral Assumptions[a], Computed with the *Chandra* Cycle 8 Response Matrices

Γ	N_H (cm^{-2})	Factor[b]
Soft Band		
1.4	Galactic	1.87
1.7	Galactic	1.81
2.0	Galactic	1.75
1.4	10^{22}	2.12
2.0	10^{22}	2.15
Full Band		
1.4	Galactic	0.75
1.7	Galactic	0.89
2.0	Galactic	1.04
1.4	10^{22}	0.51
2.0	10^{22}	0.71
Hard Band		
1.4	Galactic	0.38
1.7	Galactic	0.43
2.0	Galactic	0.47
1.4	10^{22}	0.36
2.0	10^{22}	0.45

Notes.
[a] $\Gamma = 1.4$, N_H = Galactic used for catalog fluxes.
[b] conversion factor CF where $Flux = B_{\rm rate}/(CF*10^{11})$, in units of counts erg^{-1} cm^2.

($> 5\sigma$) deviation from the quiescent background level (see Table 3).

Particular care was taken in the rejection of cosmic-ray afterglows.[45] When a cosmic ray hits a CCD pixel a residual charge can remain localized for tens of seconds and produce "afterglow events," that appear to be X-ray events, at one location for several consecutive CCD frame readouts (POG Section 6.9). To reject cosmic ray afterglows we used the CIAO tool ACIS_RUN_HOTPIX[46] and enabled VF mode background processing in ACIS_PROCESS_EVENTS. This process was successful as none of the C-COSMOS sources subsequently detected have the time localization characteristic of a spurious afterglow source. This procedure also gave a 25%–30% background reduction in the 0.5–7 keV band.

The residual background is very stable over the full field of view at $\sim 1.8 \times 10^{-7}$ counts s^{-1} $pixel^{-1}$ or $\sim$2 counts/200 ks over a 2 arcsec radius circle, which represents the typical size of our detection cell across the field. Following Alexander et al. (2003), in which the transition between a photon limited and a background limited regime is defined as >3.3 background counts per detection cell for S/N = 3, we conclude that C-COSMOS is photon limited for point source detection.

4.2.2. Exposure Maps and Sensitivity Curve

We constructed exposure maps using the standard CIAO tool sequence of ASPHIST, MKINSTMAP, and MKEXPMAP, for each ObsID on a per-CCD basis, in each of three energy bands, S, H, F.

Figure 4 (right panel) shows a composite image of the effective exposure time (s) in the soft band. We clearly see the central region with four overlapping pointings, the side strips with two observations, and the corners covered by just one pointing. The uniformity of the exposure in the central region is shown by the histogram of the exposure times shown in Figure 7. This histogram shows narrow peaks at the 1, 2, and 4 exposure values, which have Gaussian sigmas of 12.9, 13.6, and 19.3 ks, respectively, i.e., a 12% spread on the central region exposure. The total effective exposure in the inner, 4 exposure, region is $\sim$160 ks at the peak, and $\sim$170 ks at the mean, in the same region (see Figure 7).

The C-COSMOS sky coverage (i.e., the area covered as a function of limiting sensitivity) was computed in the three standard energy bands F, S, H using the exposure maps, the background maps and assuming a spectrum with $\Gamma = 1.4$ and $N_H = N_H$ (Galactic). The sky coverage in the soft band is shown in Figure 3. More details on the full band and hard band are given in Paper II (Section 7).

The main uncertainty in the estimated sky coverage comes from the range of conversion factors from count rates to fluxes induced by the variety of intrinsic X-ray spectra in the X-ray population, in both power-law slope and intrinsic absorption, at a minimum. More complex spectra are surely present. An additional complication is that the average spectral properties are a function of the observed flux (Brandt & Hasinger 2005). To estimate this uncertainty, we calculated the sky coverage for power-law spectra with $\Gamma = 1.4$ and 2.0 with Galactic N_H, and for absorbed power-law spectra with $\Gamma = 1.4$ and 2.0 and $N_H = 10^{22}$ cm^{-2}. The range of conversion factors, given by PIMMS,[47] is a factor 2.0 in the F band, 1.3 in the H band and 1.2 in the S band (Table 4). As expected from the large width of the full band, the uncertainty for the full band is larger than for the soft and hard bands.

[45] http://cxc.harvard.edu/ciao/why/afterglows.html
[46] http://cxc.harvard.edu/ciao3.4/ahelp/acis_run_hotpix.html
[47] http://cxc.harvard.edu/toolkit/pimms.jsp

Table 5
Number of Sources Detected in Each Band at the Two Adopted Thresholds

Band	$detml \geqslant 10.8$	$6 < detml < 10.8$
Full (F)	1655	71
Soft (S)	1340	88
Hard (H)	1017	165

Table 6
Number of Sources with $detml \geqslant 10.8$ in at Least One Band

Bands	Number of Sources
F+S+H	922
F+S	474
F+H	257
F	73
S	32
H	3
Total	1761

5. POINT SOURCE CATALOG

5.1. Overview

In this catalog we report the 1761 sources detected down to a defined threshold in at least one band. The threshold was chosen to balance completeness (the fraction of true sources detected) against reliability (the fraction of false sources detected). Paper II describes simulations that allowed us to choose a threshold which has a known completeness and reliability. We chose a probability threshold of $P = 2\times 10^{-5}$, giving 99.8% reliability for sources with more than 12 counts and 99.7% reliability for sources with 7 counts. This implies ∼3–5 spurious F-band detections in the full field with > 12 counts and 5 spurious detections with > 7. At this threshold, the simulations then show that C-COSMOS is 87.5% complete for 12 count sources and 68% complete for 7 count sources. The C-COSMOS false source rates are consistent with those of other surveys (e.g., AEGIS-X, Laird et al. 2008) once the higher C-COSMOS threshold and larger average source extraction region are taken into account (see Paper II, Sections 6, 8, and 9).

The maximum likelihood statistic $detml = -ln(P) = 10.8$ for $P = 2 \times 10^{-5}$, and this threshold *detml* was applied in EMLDETECT. The numbers of source detections at or above $detml = 10.8$ are listed in the left column of Table 5. Cross-matching the sources with $detml > 10.8$ in the three bands gives a total of 1761 sources. There are numerous sources with $detml > 10.8$ in fewer than three bands. In these cases we can search for significant flux in the other bands to a 100 times higher P, as the area being searched is now 100 times smaller than the whole survey area (for a 5″ cross-match radius). This corresponds to a threshold $detml = 6$. In the right-hand column of Table 5 we give the numbers of sources detected in each band having $6 < detml < 10.8$. Table 6 reports the numbers of catalog sources at or above $detml = 10.8$ in three bands, two bands, or in only one band. (In this last case the sources must have $detml > 10.8$ in order to have been selected at all.)

Almost a thousand (946) *XMM*-COSMOS sources have also been observed by *Chandra* with an exposure larger than 30 ks (Cappelluti et al. 2009), and 876 are present in the C-COSMOS catalog. Only 70 sources are not present in the *Chandra* catalog, while 24 *XMM*-COSMOS sources have been resolved into two separate sources (M. Brusa et al. 2009, in preparation; Paper III) due to the better *Chandra* PSF. Of the 70 sources not recovered by *Chandra*, more than half are in regions with low exposure (between 30 and 50 ks) as, for example, in small gaps of low exposure (Figure 4). The remainder are either sources with only hard *XMM* detections or, after a visual inspection, they are found to be spurious *XMM* sources, in agreement with the expected fraction of spurious sources. C-COSMOS and *XMM*-COSMOS combine to give a total of ∼2800 unique COSMOS X-ray sources. The distribution of X-ray fluxes for the C-COSMOS sources in the soft and hard bands is shown in Figure 8. For comparison, we also show the flux distribution of CDFN (dotted line), CDFS (dot-dashed line), and *XMM*-COSMOS detected sources (dashed line). The *Chandra* and *XMM-Newton* surveys are complementary in that, together, they span almost 3 orders of magnitude in X-ray flux, and have over 100 soft band (and over 50 hard band) sources per 0.16 dex bin over about 1.5 orders of magnitude in flux. The well-defined cutoff in source numbers at faint fluxes, which reflects the tight exposure time distribution (Figure 7), is significantly different from the relatively flat distribution of CDFN (dotted line) and CDFS (dot-dashed line) source fluxes (Figure 8).

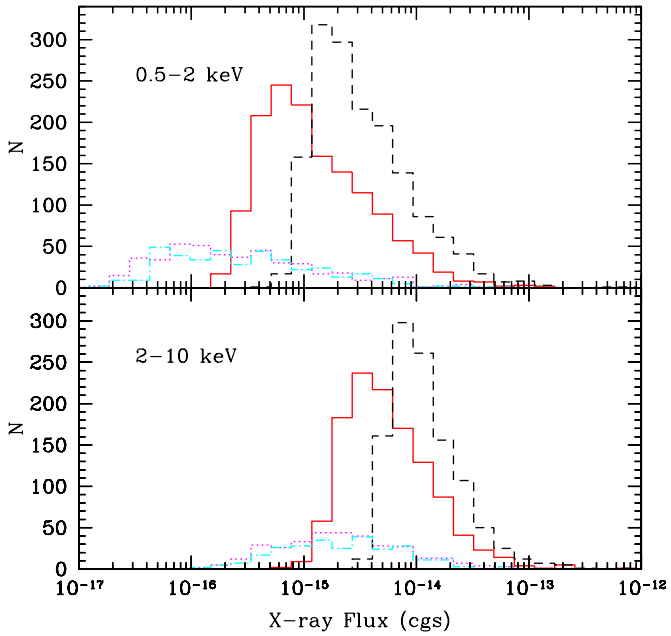

Figure 8. Distribution of fluxes for sources detected in the soft and hard band (continuous line) compared with the flux distribution of CDFN sources (dotted line), CDFS (dot-dashed line), and *XMM*-COSMOS sources (dashed line). Sources with upper limit have not been included in this figure.

(A color version of this figure is available in the online journal.)

The complete catalog contains source positions and source count rates, exposure times, signal-to-noise ratio (S/N), and fluxes in the three bands and hardness ratios (see the next section). The catalog is ordered with the sources detected in the full band first, followed by those detected in the soft band only and by those detected in the hard band only.

The resulting catalog is available in the electronic version of the journal and on the "*Chandra* COSMOS Survey" Web site.[48] Supporting data products (including images, event files and exposure maps) will be available at the "*Chandra* COSMOS Survey" Web site and at IRSA.[49] At the *Chandra* COSMOS Survey it will also be possible to browse a database that includes

[48] http://chandracosmos.cfa.harvard.edu/reports/analysis/20090310_TA_source_catalog_2.1/
[49] http://irsa.ipac.caltech.edu/data/COSMOS/

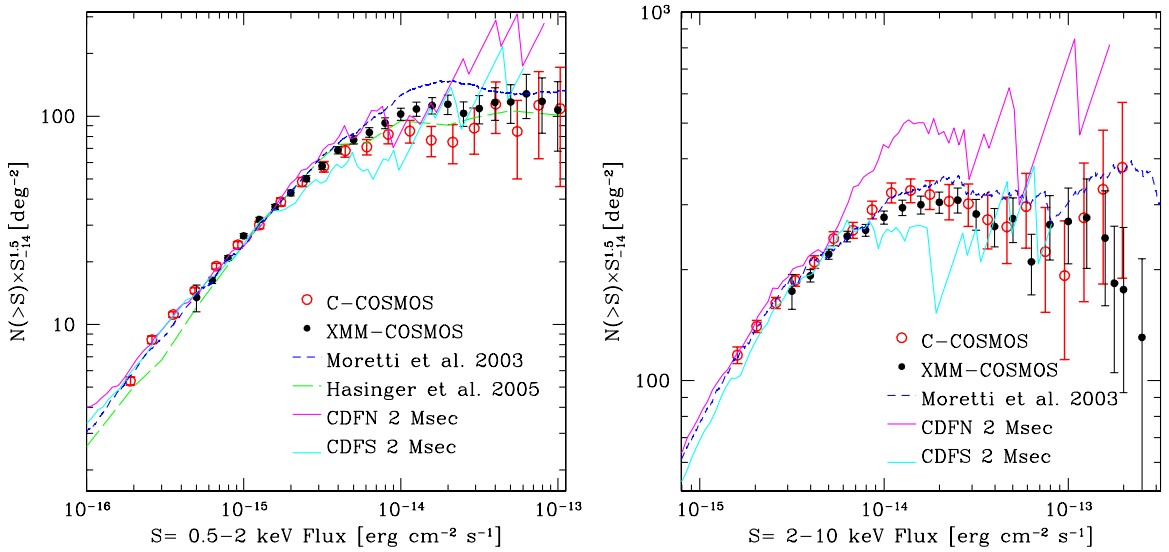

Figure 9. Euclidean-normalized, log$N$–log$S$ curves for C-COSMOS sources with *detml* >10.8: left: soft band (0.5–2 keV, red open circles), right: hard band (2–10 keV). The *XMM*-COSMOS curve (black filled circles, Cappelluti et al. 2009), the soft band curve of Hasinger et al. (2005; green line), the Moretti et al. (2003) compilation (blue dashed line), and the CDF-N (magenta solid line, Alexander et al. 2003) and CDF-S (cyan solid line, Luo et al. 2008) curves. The agreement is good over the flux interval where the various surveys have good statistics (see text).

"postage stamps" of the X-ray data for each source, along with the multiwavelength optical and infrared data, including the *I*-band, *K*-band, and *Spitzer* 3.6 μm (Band 1) images used in Paper III to identify the sources.

5.2. Catalog Description

The EMLDETECT procedure was run on the three bands: soft, hard, and full. In order to be consistent with other results in literature, count rates estimated in the 2–7 keV and 0.5–7 keV energy bands were extrapolated into 2–10 keV and 0.5–10 keV fluxes, respectively, using a spectral slope, $\Gamma = 1.4$. We also report the number counts obtained from aperture photometry (see Paper II).

Table 7 gives the columns of the catalog of the 1761 X-ray sources. A more detailed description of each column is reported below.

1. Column 1: *Chandra* source name, following the standard IAU convention with the prefix "CXOC" for "*Chandra* X-ray Observatory COSMOS" survey.
2. Column 2: source number. Sources are listed in order of detection: first those detected in the full band with *detml* $\geqslant$ 10.8, followed by those detected in the soft band only and by those detected in the hard band only.
3. Columns 3–4: right ascension and declination in the J2000 coordinate system.
4. Column 5: positional error ($\sqrt{\sigma^2_{\rm R.A.} + \sigma^2_{\rm decl.}}$) computed using the following equation $\mathrm{Pos_{error}} = \mathrm{PSF_{radius}}/\sqrt{S}$, where S is the number of net source counts, after the subtraction of the background, in a circular region of radius corresponding to the 50% encircled energy in the field where the source is at the lowest off-axis angle (Paper II).
5. Column 6–7: count rate and count rate error in the full band (0.5–7 keV). These are *effective* count rates that would apply if the source had been observed at the aim point in every pointing, i.e., computed by dividing the best fit counts for each source by the effective exposure time at the position of each source (the effective exposure time includes

Table 7
Data Fields in the Catalog

No.	Field	Note
1	NAME	*Chandra* source name
2	Source #	source number.
3	R.A.	*Chandra* Right Ascension (J2000, hms)
4	DEC	*Chandra* Declination (J2000, dms)
5	pos_err	Positional error [arcsec]
6	f_rate	0.5–7 keV count rate (counts s^{-1})
7	f_rate_err	0.5–7 keV count rate error (counts s^{-1})
8	f_flux	0.5–10 keV Flux [erg cm^{-2} s^{-1}]
9	f_flux_err	0.5–10 keV Flux error [erg cm^{-2} s^{-1}]
10	f_snr	0.5–7 keV S/N Ratio
11	f_exptime	0.5–7 keV exposure time [ks]
12	f_cts_ap	0.5–7 keV aperture photometry net counts [counts]
13	f_cts_ap_err	0.5–7 keV aperture photometry net counts error [counts]
14	f_exptime_ap	0.5–7 keV exposure time from aperture photometry [ks]
15	s_rate	0.5–2 keV count rate (counts s^{-1})
16	s_rate_err	0.5–2 keV count rate error (counts s^{-1})
17	s_flux	0.5–2 keV Flux [erg cm^{-2} s^{-1}]
18	s_flux_err	0.5–2 keV Flux error [erg cm^{-2} s^{-1}]
19	s_snr	0.5–2 keV S/N Ratio
20	s_exptime	0.5–2 keV exposure time [ks]
21	s_cts_ap	0.5–2 keV aperture photometry net counts [counts]
22	s_cts_ap_err	0.5–2 keV aperture photometry net counts error [counts]
23	s_exptime_ap	0.5–2 keV exposure time from aperture photometry [ks]
24	h_rate	2–7 keV count rate (counts s^{-1})
25	h_rate_err	2–7 keV count rate error (counts s^{-1})
26	h_flux	2–10 keV Flux [erg cm^{-2} s^{-1}]
27	h_flux_err	2–10 keV Flux error [erg cm^{-2} s^{-1}]
28	h_snr	2–7 keV S/N Ratio
29	h_exptime	2–7 keV exposure time [ks]
30	h_cts_ap	2–7 keV aperture photometry net counts [counts]
31	h_cts_ap_err	2–7 keV aperture photometry net counts error [counts]
32	h_exptime_ap	2–7 keV exposure time from aperture photometry [ks]
33	hr	hardness ratio
34	hr_lim_lo	hardness ratio 90% lower limit
35	hr_lim_hi	hardness ratio 90% upper limit

Note. The C-COSMOS Bright Source Catalog is available in the electronic version of the journal.

corrections for vignetting, dither, bad pixels and spatially dependent quantum efficiency). The count rate error at 68% confidence level was computed using the equation error $== \frac{\sqrt{C_{s,90\%}+(1+a)B_{90\%}}}{0.9 \cdot T}$, where C_s are the source counts estimated by *EMLdetect*, corrected to an area including 90% of the PSF,[50] B are the background counts evaluated from the background rate (counts pixel^{-1}) estimated by *EMLdetect* multiplied for an area of radius R_w, which is the mean of the radii, corresponding to 90% enclosed counts fraction (ECF) of each observation, weighted by the observation exposure relative to the total exposure, and T is the vignetting corrected exposure time at the position of the source from the exposure maps. We use $a = 0.5$, to allow for uncertainties in the background, which is computed through the EMLDETECT procedure (see Paper II for more details).

6. Column 8–9: full band 0.5–10 keV fluxes and errors were computed converting count rates to fluxes using the following formula: $Flux = B_{\rm rate}/(CF * 10^{11})$, where $B_{\rm rate}$ is the count rate in each band as described in Column 6, CF is the energy conversion factor 0.742 counts erg^{-1} cm^2 (and 1.837 and 0.381 for the soft and hard, 2–10 keV band respectively) appropriate for a power-law spectrum with spectral index $\Gamma = 1.4$ and Galactic column density $N_H = 2.7 \times 10^{20}$ cm^{-2}. For sources not detected in this band, a 90% upper limit is reported (see Paper II for details).
7. Column 10: full band signal-to-noise ratio.
8. Column 11: full band exposure time derived from the exposure map.
9. Column 12–13: the aperture photometry counts and error in the full band (0.5–7 keV) are derived from event data for each individual Obsid and CCD where a source lands. Note that $(F\_rate \times f\_exptime) \neq f\_cts\_ap$. Circular extraction regions corresponding to the 90% ECF for that observation are centered on the source R.A., decl. The individual photometry values are then merged to produce a single set of values accounting for the ECF for each ObsID, given the different extraction regions needed.
10. Column 14: exposure time (ks) from the same region used to generate the aperture photometry.
11. Column 15–23: same as Columns 6–14 for the soft band (0.5–2 keV).
12. Column 24–32: same as Columns 6–14 for the hard band (2–7 keV). Fluxes and errors are computed for the 2–10 keV band with the conversion factor quoted above.
13. Column 33–35: hardness ratio and 90% upper and lower errors computed as follows: H−S/H+S, where H are the counts in the hard band and S the counts in the soft band. The hardness ratio was calculated starting with the EMLDETECT rate values. Upper and lower limits were calculated using the Bayesian estimation of hardness ratio code (BEHR; Park et al. 2006). Pseudo-source and background count values were generated using the net count rate, background rate (per pixel), and a 3 arcsec source aperture and 5–20 arcsec aperture for background areas. The aperture photometry was unsuitable for this purpose because the individual extraction apertures do not have the constant background/source area ratios required by the assumptions used in BEHR.

[50] http://cxc.harvard.edu/caldb/

5.3. Catalog Completeness and Number Counts

In order to provide an end-to-end check that the many calibration steps taken in deriving the *Chandra* COSMOS point source catalog have been performed correctly, we constructed the observed log$N$–log$S$ curve, i.e. the number of sources, $N(>S)$, detected per square degree brighter than a given flux, S (erg cm^{-2} s^{-1}) in the soft (0.5–2 keV) and hard (2–10 keV) bands. Because at the limiting fluxes the sky coverage is small (Figure 3), and so has a large fractional error, we used the flux limits given in Table 1, Column 3, thus omitting the faintest ∼10 sources. X-ray source counts in this flux and energy range have been well studied, giving us a good baseline against which to compare C-COSMOS (Cappelluti et al. 2009).

The results for sources detected at *detml* >10.8 (Table 5, left column) are shown in Figure 9, normalized by a Euclidean 1.5 slope to enable differences between various X-ray log$N$–log$S$ curves to be seen easily. Figure 9 also shows comparisons with several other log$N$-log$S$ curves: from Moretti et al (2003, blue dashed line), which combines data from *ROSAT* (for bright sources), *XMM-Newton* (for intermediate flux sources), and *Chandra* for faint sources; from Hasinger et al. (2005) log$N$–log$S$ (green dashed line); and from the CDF-N (magenta solid line; Alexander et al. 2003) and CDF-S (cyan solid line; Luo et al. 2008) curves. In the range where these curves overlap and C-COSMOS has good statistics the agreement is excellent, and C-COSMOS extends a factor ∼4 below the *XMM*-COSMOS limit, as expected.

In the soft band, around $\sim 2 \times 10^{-14}$ erg cm^{-2} s^{-1}, the C-COSMOS log$N$–log$S$ shows a ∼20%–30% underdensity at a 2σ level with respect to the *XMM*-COSMOS source counts. In order to evaluate this deviation, we estimated the amplitude of the fluctuations expected due to sample and cosmic variance. According to Yang et al. (2004, 2006) and Cappelluti et al. (2009), the fluctuations of the counts in a box of area Ω deg^2 of a population of $\mathcal{N}$ deg^{-2} sources at a given flux limit is given by a linear combination of a Poisson fluctuations and a cosmic variance component introduced by source clustering:

$$\sigma_{cv}^2 = \mathcal{N} + \frac{\mathcal{N}}{\Omega^2} \int w(\theta) d\theta_1 d\theta_2. \quad (1)$$

In Equation (1) $w(\theta)$ is the angular autocorrelation function expressed as a $w(\theta) = \frac{\theta}{\theta_0}^{-\gamma}$. According to Cappelluti et al. (2007), Equation (1) can be solved analytically by knowing the slope and the amplitude of $w(\theta)$. By using the source surface density of soft X-ray sources at 2×10^{-14} erg cm^{-2} s^{-1} (i.e., ∼30 source deg^{-2}) on a box of 0.9 deg^2, and assuming the angular autocorrelation function of Miyaji et al. (2007) for *XMM*-COSMOS (i.e., $\theta_0 = 2''$, $\gamma = 1.8$), we determined $\sigma^2 \sim 36$ which corresponds to a fraction variance of 20% of the source counts. We can therefore conclude that a deviation of the size observed can be introduced by a single structure, in an area of *XMM*-COSMOS not covered by *Chandra*, that generates a fluctuation in the bright source counts at 1.5σ level.

Another check of the source detection efficiency at the brighter C-COSMOS flux levels is a comparison with the *XMM* COSMOS survey (Hasinger et al. 2007). As shown by Cappelluti et al. (2009) and M. Brusa et al. (2009, in preparation), C-COSMOS recovers ∼93% of the *XMM* sources in the C-COSMOS field, resolving ∼3% into close pairs.

6. CONCLUSIONS AND FUTURE WORK

We have presented the ∼0.9 deg^2 *Chandra* COSMOS survey (C-COSMOS) and a catalog of point sources from that survey. Employing a heavily overlapping tiling of ACIS-I observations has proven an effective method of covering a large area to a well-defined exposure (±12%) and uniform flux limit. The central ∼0.5 deg^2 achieved an exposure of 160 ks, and the outer ∼0.4 deg^2 achieved an exposure of ∼80 ks. The equatorial location of COSMOS helped to produce a uniform tiling pattern by allowing an almost constant roll angle for *Chandra* observations over most of the target visibility window. The point source catalog from the C-COSMOS survey has a flux limit of 2×10^{-16} erg cm^{-2} s^{-1} (0.5–2 keV) and contains 1761 sources detected in at least one band with a probability of being spurious of $<2 \times 10^{-5}$ (*detml* $\geqslant$ 10.8).

The novel three-stage source detection method employed (Paper II) coped well with the peculiarities of the C-COSMOS tiling scheme and, more generally, is good at separating close pairs of sources, while retaining photometric accuracy. The C-COSMOS sky coverage has a sharp cutoff which produces a homogeneous flux threshold over the whole area and the soft band log$N$–log$S$ curve for C-COSMOS matches well the Hasinger et al. (2005) determination over a broad flux range, giving us high confidence in the completeness of the catalog down to the limiting flux.

The catalog is available in the electronic version of the journal and on the "*Chandra* COSMOS Survey" Web site[48] Supporting data products (including images, event files and exposure maps) are available at the "*Chandra* COSMOS Survey" Web site and at IRSA.[49]

The subarcsecond accuracy of the *Chandra* positions, together with the rich pre-existing deep multiwavelength coverage of the COSMOS field, allows us to reach a 96% identification rate for the C-COSMOS sources with counterparts in both optical and infrared, and 99.7% in at least one band (Paper III).

A parallel effort on the detection of extended sources in the C-COSMOS field finds ∼50 groups and clusters (A. Finoguenov et al. 2009, in preparation).

We anticipate a rich haul of science results from C-COSMOS. The *Chandra* sources have already resolved ambiguous source identifications from the *XMM*-COSMOS survey (Hasinger et al. 2007, Brusa et al. 2007, 2008, Cappelluti et al. 2007, 2009). The paper by Fiore et al. (2008) on the stacking analysis of sources with extreme mid-infrared-to-optical ratio, presumably Compton-thick AGNs, has been recently accepted. Several further papers are in preparation or submitted on off-nuclear sources in galaxies (Mainieri et al. 2009), X-ray source correlation functions (Miyaji et al. 2007), the three-dimensional cluster/AGN cross-correlation function (Cappelluti et al. 2009), high X-ray/optical flux ratio objects (F. Civano et al. 2009, in preparation), high-redshift QSO (F. Civano et al. 2009, in preparation), and other topics.

A basic X-ray spectral analysis of the nearly 500 sources with more than 80 counts (∼23% of the total sample) becomes possible. The resulting spectral slopes and absorbing column densities will allow the statistical properties of a large sample at substantial redshift and over a uniform and contiguous field to be studied effectively (G. Lanzuizi et al. 2009, in preparation).

There is information in C-COSMOS below the current catalog flux limit, thanks to the low background of *Chandra* ACIS. A "stacking" analysis (Brusa et al. 2002; Hornschemeier et al. 2002, 2003) allows the mean X-ray properties of groups of objects to be determined. Miyaji et al. (2007) have solved the issues created by the C-COSMOS tiling scheme for stacking and papers using this tool are in preparation on $z \sim 1$ elliptical galaxies (Kim et al. 2007). The potential uses of stacking in the C-COSMOS field are extensive, thanks to the multiple data sets available from which to choose samples for stacking. For example, there will be $\sim 2 \times 10^4$ galaxies with good optical spectra from z-COSMOS (Lilly et al. 2007) in the C-COSMOS field. This entire sample is well characterized both morphologically via *HST* imaging, and in terms of stellar population, from the UV to far-IR coverage of the other telescopes that have observed COSMOS (Scoville et al. 2007b). This rich data set will enable galaxy X-ray evolution studies by environment, morphology, and luminosity using fine-grained stacks of C-COSMOS data with ∼100 galaxies per bin, for an effective exposure time of ∼20 Ms per bin.

Clearly the C-COSMOS survey will be of value for some time.

We thank the *Chandra* mission planning team, especially Pat Slane and Jan Vrtilek, and the *Chandra* pipeline data processing team for the extraordinary efforts they put into the successful scheduling and execution of C-COSMOS. We also thank the rest of COSMOS team whose support has been invaluable in reaching this stage. We thank Bin Luo for sensitivity curves of *Chandra* Deep Fields. We gratefully thank the *Chandra* EPO team, in particular Eli Bressert, for creating the true color X-ray image. This research has made use of data obtained from the *Chandra* Data Archive and software provided by the *Chandra X-ray Center* (CXC) in the application packages CIAO and Sherpa.

This work was supported in part by NASA *Chandra* grant number GO7-8136A (M.E., C.V., M.B., A.F.), NASA contract NAS8-39073 (*Chandra* X-ray Center), and by NASA/ADP grant NNX07AT02G (TM at UCSD). In Italy this work is supported by ASI/INAF contracts I/023/05/0, I/024/05/0 and I/088/06, by PRIN/MUR grant 2006-02-5203. In Germany this project is supported by the Bundesministerium für Bildung und Forschung/Deutsches Zentrum für Luft und Raumfahrt and the Max Planck Society.

REFERENCES

Alexander, D. M., et al. 2003, AJ, 126, 539
Arnaboldi, M., Neeser, M. J., Parker, L. C., Rosati, P., Lombardi, M., Dietrich, J. P., & Hummel, W. 2007, Messenger, 127, 28
Bertoldi, F., et al. 2007, ApJS, 172, 132
Brandt, W. N., & Hasinger, G. 2005, ARA&A, 43, 827
Brandt, W. N., Hornschemeier, A. E., Schneider, D. P., Alexander, D. M., Bauer, F. E., Garmire, G. P., & Vignali, C. 2001, ApJ, 558, L5
Brunner, H., Cappelluti, N., Hasinger, G., Barcons, X., Fabian, A. C., Mainieri, V., & Szokoly, G. 2008, A&A, 479, 283
Brusa, M., et al. 2002, ApJ, 581, 89
Brusa, M., et al. 2007, ApJS, 172, 353
Capak, P., et al. 2007, ApJS, 172, 99
Cappelluti, N., et al. 2007, ApJS, 172, 341
Cappelluti, N., et al. 2009, A&A, 497, 635
Damiani, F., Maggio, A., Micela, G., & Sciortino, S. 1997, ApJ, 483, 350
Dickey, J. M., & Lockman, F. J. 1990, ARA&A, 28, 215
Eckart, M. E., Stern, D., Helfand, D. J., Harrison, F. A., Mao, P. H., & Yost, S. A. 2006, ApJS, 165, 19
Fabbiano, G. 2006, ARA&A, 44, 323
Ferrarese, L., & Merritt, D. 2000, ApJ, 539, L9
Fiore, F., et al. 2003, A&A, 409, 79
Fiore, F., et al. 2008, ApJ, 672, 94
Fruscione, A., et al. 2006, Proc. SPIE, 6270, 6270IV
Garmire, G. P., Bautz, M. W., Ford, P. G., Nousek, J. A., & Ricker, G. R., Jr. 2003, Proc. SPIE, 4851, 28

Gebhardt, K., et al. 2000, ApJ, 539, L13
Giacconi, R., et al. 2002, ApJS, 139, 369
Gilli, R., Comastri, A., & Hasinger, G. 2007, A&A, 463, 79
Harrison, F. A., Eckart, M. E., Mao, P. H., Helfand, D. J., & Stern, D. 2003, ApJ, 596, 944
Hasinger, G., Miyaji, T., & Schmidt, M. 2005, A&A, 441, 417
Hasinger, G., et al. 2007, ApJS, 172, 29
Hornschemeier, A. E., Brandt, W. N., Alexander, D. M., Bauer, F. E., Garmire, G. P., Schneider, D. P., Bautz, M. W., & Chartas, G. 2002, ApJ, 568, 82
Hornschemeier, A. E., et al. 2003, AJ, 126, 575
Ilbert, O., et al. 2008, ApJ, 690, 1236
Kim, M., et al. 2007, ApJS, 169, 401
Laird, E. S., et al. 2008, ApJS, 180, 102
Lehmer, B. D., et al. 2005, ApJS, 161, 21
Lehmer, B. D., et al. 2006, AJ, 131, 2394
Lilly, S. J., et al. 2007, ApJS, 172, 70
Luo, B., et al. 2008, ApJS, 179, 19
Magorrian, J., et al. 1998, AJ, 115, 2285
Mainieri, V., et al. 2009, A&A, submitted
Manners, J. C., et al. 2003, MNRAS, 343, 293
Marconi, A., & Hunt, L. K. 2003, ApJ, 589, L21
McCracken, H. C., et al. 2009, ApJ, submitted
Miyaji, T., et al. 2007, ApJS, 172, 396
Mobasher, B., et al. 2007, ApJS, 172, 117
Moretti, A., Campana, S., Lazzati, D., & Tagliaferri, G. 2003, ApJ, 588, 696
Murray, S. S., et al. 2005, ApJS, 161, 1
Nandra, K., Mushotzky, R. F., Arnaud, K., Steidel, C. C., Adelberger, K. L., Gardner, J. P., Teplitz, H. I., & Windhorst, R. A. 2002, ApJ, 576, 625
Nandra, K., et al. 2005, MNRAS, 356, 568
Park, et al. 2006, ApJ, 652, 610
Puccetti, S., et al. 2006, A&A, 457, 501
Puccetti, S., et al. 2009, ApJS, submitted
Salvato, M., et al. 2009, ApJ, 690, 1250
Sanders, D. B., et al. 2007, ApJS, 172, 86
Schinnerer, E., et al. 2007, ApJS, 172, 46
Scott, K. S., et al. 2008, MNRAS, 385, 2225
Scoville, N., et al. 2007a, ApJS, 172, 1
Scoville, N., et al. 2007b, ApJS, 172, 38
Scoville, N., et al. 2007c, ApJS, 172, 150
Taniguchi, Y., et al. 2007, ApJS, 172, 9
Tremaine, S., et al. 2002, ApJ, 574, 740
Trump, J. R., et al. 2007, ApJS, 172, 383
van Speybroeck, L. P., et al. 1997, Proc. SPIE, 3113, 89
Weisskopf, M. C., Brinkman, B., Canizares, C., Garmire, G., Murray, S., & Van Speybroeck, L. P. 2002, PASP, 114, 1
Wright, E. L. 2006, PASP, 118, 171
Yang, Y., Mushotzky, R. F., Barger, A. J., & Cowie, L. L. 2006, ApJ, 645, 68
Yang, Y., Mushotzky, R. F., Steffen, A. T., Barger, A. J., & Cowie, L. L. 2004, AJ, 128, 1501
Zamojski, M. A., et al. 2007, ApJS, 172, 468